

Lithium Niobate Thin Film Polarization Beam Splitter Based on Asymmetric Directional Coupling

Yinan Wu¹, Xuerui Sun, Hao Li, Chuanyi Lu, Yuting Zhang, Shijie Liu, Yuanlin Zheng¹, and Xianfeng Chen¹

Abstract—Polarization devices on lithium niobate thin film (LNTF) are vital components for photonic integrated circuits (PICs) on the novel platform. Because both linear and nonlinear devices on the anisotropic platform are intrinsically polarization-dependent. Here, we demonstrate compact polarization beam splitters (PBS) on LNTF based on two asymmetric directional couplers with an effective length of only 180 μm . The PBS is fabricated via a single-step electron beam lithography (EBL) and inductively coupled plasma (ICP) etching process. Our device shows efficient PBS operation at the telecom bands with an extinction ratio over 26 dB and 13 dB for fundamental TE and TM modes, respectively. The device holds promise for efficient on-chip polarization division multiplexing and polarization manipulation, which would become an indispensable component in future LNTF PICs.

Index Terms—Cross-polarizaiton coupling, directional coupler, Lithium niobate thin film, nanowaveguide, photonic intergrated circuit, polarziation device.

I. INTRODUCTION

A S A multifunctional optical material with huge potential, lithium niobate thin film (LNTF) is considered as

Manuscript received 8 July 2022; revised 17 August 2022; accepted 29 August 2022. Date of publication 1 September 2022; date of current version 20 December 2022. This work was supported in part by the National Natural Science Foundation of China under Grants 12074252, 62022058, 62005159, and 11734011, in part by the National Key Research and Development Program of China under Grants 2017YFA0303701, and 2018YFA0306301, in part by Shanghai Municipal Science and Technology Major Project under Grant 2019SHZDZX01-ZX06, in part by Shanghai Rising-Star Program under Grant 20QA1405400, and in part by Shanghai Jiao Tong University under Grant 21X010200828. (Yinan Wu and Xuerui Sun contributed equally to this work.) (Corresponding authors: Yuanlin Zheng, Xianfeng Chen.)

Yinan Wu, Xuerui Sun, Hao Li, Chuanyi Lu, Yuting Zhang, and Shijie Liu are with the State Key Laboratory of Advanced Optical Communication Systems and Networks, School of Physics and Astronomy, Shanghai Jiao Tong University, Shanghai 200240, China (e-mail: wyn_cn@sjtu.edu.cn; sxr0306@sjtu.edu.cn; lihaosky@sjtu.edu.cn; luchuanyi@sjtu.edu.cn; 302562451@qq.com; 282017047@qq.com).

Yuanlin Zheng is with the State Key Laboratory of Advanced Optical Communication Systems and Networks, School of Physics and Astronomy, Shanghai Jiao Tong University, Shanghai 200240, China, and also with the Shanghai Research Center for Quantum Sciences, Shanghai Jiao Tong University, Shanghai 201315, China (e-mail: ylzheng@sjtu.edu.cn).

Xianfeng Chen is with the State Key Laboratory of Advanced Optical Communication Systems and Networks, School of Physics and Astronomy, Shanghai Jiao Tong University, Shanghai 200240, China, also with the Shanghai Research Center for Quantum Sciences, Shanghai Jiao Tong University, Shanghai 201315, China, and also with the Collaborative Innovation Center of Light Manipulations and Applications, Shandong Normal University, Jinan 250358, China (e-mail: xfchen@sjtu.edu.cn).

Color versions of one or more figures in this article are available at <https://doi.org/10.1109/JLT.2022.3203409>.

Digital Object Identifier 10.1109/JLT.2022.3203409

a revolutionary photonic integrated platform for on-chip optical manipulation and processing [1], [2], [3], [4], [5], [6]. Light can be strongly confined in sub-micrometer waveguides, i.e., nanowaveguides, with dramatically enhanced light-matter interactions in LNTF by harnessing its high refractive index contrast between lithium niobate (LN) and silica, as well as broad transparent range, large nonlinear and electro-optic coefficients of LN. Tremendous effects have been made in the development of different devices on LNTF with superior performance for various photonics applications [7], [8], [9], [10], [11], [12], [13], [14], [15]. Within the last few years, a variety of excellent electro-optic modulators [7], [16], [17], [18], [19], [20], [21], frequency converters [8], [9], [10], [11], [12], parametric oscillators [22], frequency comb generators [13], [23], [24], supercontinuum generators [14], [25], and quantum sources [9], [15] has been successfully demonstrated, with performance far beyond the limit of their conventional counterparts. With the multifunctionality of LN, different functional devices are to be incorporated in photonic integrated circuits (PICs) on the same chip in the future. Devices for wavelength, mode, and polarization-division multiplexing [26], [27], [28], [29] are thus becoming more and more desired and urgent.

Lithium niobate itself is an anisotropic crystal, which makes devices on LNTF intrinsically polarization dependent. Other than polarization-division multiplexing applications, the electro-optic effect and second-order nonlinear wave mixings are also polarization sensitive. Besides, devices with small footprints are more favorable in dense integration. To these ends, high-capacity yet compact polarization manipulators like polarization beam rotators (PBR) and polarization beam splitters (PBS) that harness the polarization degree of freedom are greatly sought after for LNTF PICs. Polarization devices on LNTF will greatly expand the toolbox on the novel platform. So far, several PBR on LNTF with different structure and design have been reported [30], [31], [32], but fewer PBS [33], [34], [35], [36] have been demonstrated. And they still rely on complex design and structures.

Here, we demonstrate a compact PBS on LNTF based on two asymmetric directional couplers (ADCs) via two-stage mode conversion processes. The whole device only requires a simple fabrication process, i.e., a single-step EBL and ICP etching. The PBS, with a reduced length of 180 μm , shows broadband operation in the telecom bands. A high polarization extinction ratio (PER) and low insertion loss is achieved. The experimentally measured PER from 1520 nm to 1570 nm is 26 dB for

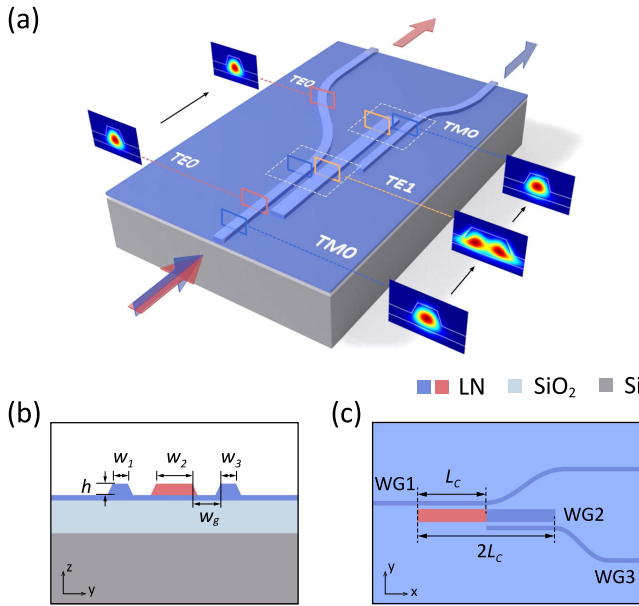


Fig. 1. (a) Schematic illustration of the PBS on LNTF with numerically simulated eigenmodes in each waveguide. (b) Cross section and (c) top view of the PBS.

fundamental TE (TE₀) and 13 dB for fundamental TM (TM₀) input, respectively.

II. NUMERICAL SIMULATION

Fig. 1(a) depicts the illustration of our PBS on the 800-nm thick z-cut LNTF platform. The LNTF sits on top of a 2-μm-thick SiO₂ buffering layer and 500-μm-thick Si substrate. The PBS is designed to split the input modes into two output ports, i.e., through port for TE₀ and cross port for TM₀, respectively. As shown in Fig. 1(b) and 1(c), the mode splitting section of the device consists of three ridge waveguides, denoted as WG1, WG2, and WG3 with different widths of \$W_1\$, \$W_2\$, and \$W_3 = W_1\$, respectively. The two ADCs are formed between WG1 and WG2, WG2 and WG3. The coupling gap is the same and is denoted as \$W_g\$. In the numerical simulation, the etching depth, \$h\$ is set to be 450 nm and the etching angle is 63.5°, consistent to the actual etching condition. In addition, a S-bend waveguide is placed at the end of each ADC to avoid mode coupling and separate the two output ports for experimental investigation. For TM₀ mode input, the first directional coupling (DC1) process occurs between WG1 and WG2. Under the phase matching condition, a wider waveguide WG2 is used to mediate converting the TM₀ mode in WG1 into a higher-order mode in WG2 (TE₁ in our case). Regarding the second directional coupling (DC2) process, we set WG3 the same width of WG1 to transfer the mode in WG2 back to TM₀ under the same phase matching condition as DC1. The phase matching condition is invalid for TE modes. So that the TE₀ mode propagates directly to the through port without mode coupling. In other words, for the TM mode, there are two asymmetric directional coupling occurring during the whole process.

The wider waveguide WG2 serves as a bridge to help the TM₀ mode coupling from WG1 to WG3. As shown in Fig. 1(c),

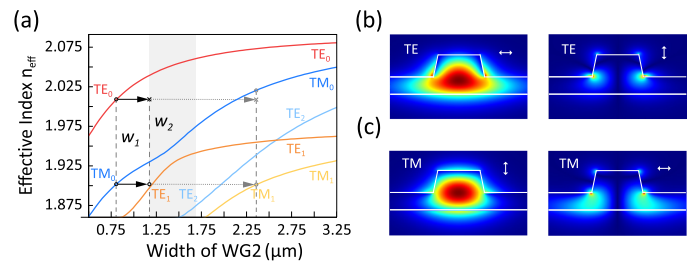


Fig. 2. (a) Effective refractive indices for the lowest-order modes at the wavelength of 1550 nm with respect to the waveguide width. The distributions of different electric field components (not to scale) of (b) quasi-TE and (c) quasi-TM modes in the ridge waveguide.

the directional coupling length \$L_c\$, i.e., the length required for a complete coupling from one mode to another, needs to be optimized. In the PBS device, two symmetrical directional coupling processes are required to complete the polarization splitting, thus the length of the WG2 should be set to be twice the coupling length. The effective length of the PBS is \$2L_c\$. And the overall high performance of the PBS requires that the parameters of the width of the waveguides \$W_1\$, \$W_2\$, and \$W_3 = W_1\$, the coupling gap \$W_g\$, and the coupling length \$L_c\$ be optimized simultaneously.

Fig. 2(a) illustrates the calculated effective refractive indices (\$n_{eff}\$) of the five lowest-order eigenmodes in the LN ridge waveguide. Firstly, the input/output waveguide needs to support only fundamental modes. The existence of high-order modes not only badly influences the mode coupling, but also is unwanted in actual applications. It is found that waveguides narrower than 0.8 μm supports only TE₀ and TM₀ modes in the telecom bands. As marked by the horizontal solid arrows, one can see that the TM₀ mode in WG1 and the TE₁ mode in WG2 are phase matched when \$W_1 = 0.8 \mu\text{m}\$, \$W_2 = 1.17 \mu\text{m}\$. However, under the same condition, there is no mode in WG2 to match the TE₀ mode in WG1. So the TE₀ mode will propagate straight forward along the waveguide without any mode coupling. A similar condition also exists when \$W_1 = 0.8 \mu\text{m}\$, \$W_2 = 2.33 \mu\text{m}\$, as marked by the horizontal dotted arrows. The TM₀ mode in WG1 matches with the TM₁ mode in WG2. But the TE₀ mode in WG1 is also in close phase matching with the TE₁ mode in WG2. In this situation, both the TE₀ mode and TM₀ mode in WG1 would couple into WG2 leading to mode hybridization and efficient polarization splitting cannot be realized.

It is worth mentioning that the eigenmodes are not ideally pure TE or TM modes in general, but quasi-TE or quasi-TM modes. Fig. 2(b) and 2(c) show the distribution of the vertically and horizontally polarized components of the quasi-TE₀ and TM₀ modes in the ridge waveguide, respectively. Thus, mode conversion between TE and TM modes can be realized during directional coupling, i.e., cross-polarization coupling [37]. In the conditions as marked by the gray area in Fig. 2(a), mode hybridization dominates, as TM₀ mode and TE₁ mode are hybridized in this region [38]. In general cases, one can obtain stronger cross-polarization coupling when the conditions are close to the mode hybridization area. This feature is utilized during the directional coupling as described previously.

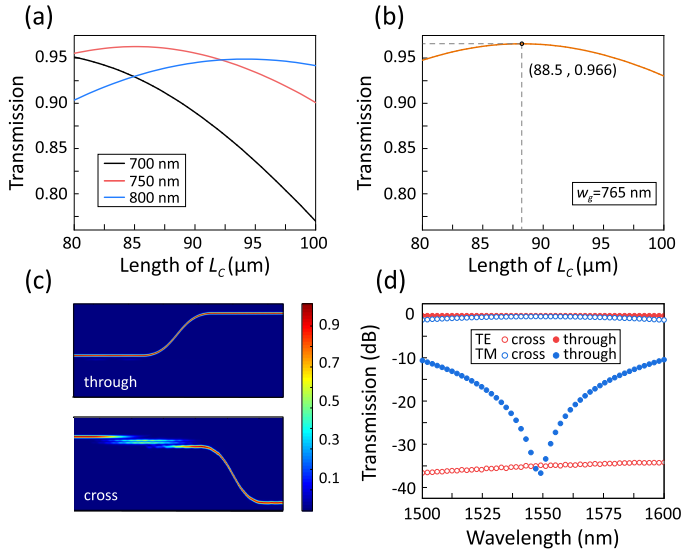


Fig. 3. (a) Efficiencies of coupling from the TM₀ mode in WG1 to the TE₁ mode in WG2 with respect to the directional coupling length L_c at different coupling gaps W_g . (b) Coupling efficiency with respect to L_c when $W_g = 765$ nm. (c) Light propagation for the TE (through) and TM (cross) modes at 1550 nm. (d) Transmission spectra of the through and cross ports.

After optimizing the waveguide widths, the coupling length L_c and the waveguide gap W_g are to be determined. At the end of the DC1 and DC2, a S-bend waveguide is introduced to separate the two ports for the convenience during experimental measurement. It should be enough-long to avoid bending loss. The footprint of the S-bend waveguide is $20 \times 100 \mu\text{m}^2$ in our design. A mode expansion monitors are placed at the end of output waveguides to determine the PBS transmission spectra. To obtain the highest coupling efficiency from TM₀ mode in WG1 to TE₁ mode in WG2, the L_c is determined by calculating the coupling efficiency under different coupling gaps W_g at the wavelength of 1550 nm. The effective length of the PBS is twice of L_c with maximum coupling efficiency. The highest coupling efficiency reaches 95% when W_g is in the range of 700–800 nm, as shown in Fig. 3(a). To appropriately reduce the length of L_c while achieving high coupling efficiency, W_g is optimized to be 765 nm. The corresponding L_c is 88.5 μm and the conversion efficiency is 96.6%, as shown in Fig. 3(b). Because the PBS contains two ADCs, the length of the bridge waveguide WG2 should be twice of L_c to transfer the TE₁ mode back into the TM₀ mode in WG3, i.e., two-stage mode conversion processes. As can be seen, the designed device footprint is smaller than those based on adiabatically tapered structures [8]. The theoretical coupling efficiency does not equal to unity due to the cross-polarization coupling of quasi modes, since mode expansion monitors only collect the energy of pure TE and TM modes.

Fig. 3(c) shows the simulated light propagation along the PBS device when inputting the TE₀ and TM₀ mode, respectively. Fig. 3(d) shows the calculated port transmission spectra for TE and TM modes over the bandwidth of 1500–1600 nm. As can be seen, TM modes has a moderate wavelength sensitivity due to the two-stage mode conversion process. Still, the polarization extinction ratio (PER) for TE and TM inputs exceeds 35 dB and

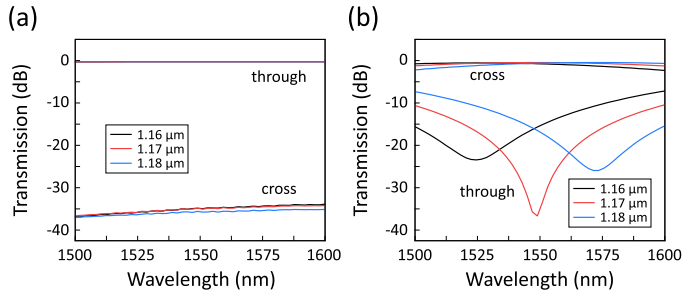


Fig. 4. Transmission spectra for (a) TE and (b) TM mode input with different W_2 .

20 dB spanning from 1530 to 1560 nm, inferring that the PBS has a high polarization splitting capacity over a wide bandwidth.

Considering the manufacturing process tolerance, the performance of the PBS is investigated by altering the width of the bridge waveguide WG2, W_2 , from 1.16 to 1.18 μm , as shown in Fig. 4. It can be seen that WG2 has a great impact on the overall performance of the device. When the width of the WG2 gets narrower, the center wavelength of the PBS has a red shift. Overall, the TM₀ modes are more sensitive to the structural variation than TE₀ ones, because TM modes undergo directional coupling twice while TE modes do not. However, for the wavelength spanning from 1520–1570 nm, the PER of TE₀ and TM₀ modes is still higher than 35 dB and 10 dB, respectively, despite a width discrepancy of ± 10 nm. This implies a relatively large fabrication tolerance during the precision nanofabrication process. As a comparison, similar devices based on adiabatically tapered structures would possess a larger tolerance, but they require a much longer length which is a disadvantage in dense integration [30], [31]. While for other schemes, such as interferometer, metasurface, slot waveguides, and heterogeneous integration, higher precision and more complex fabrication processes are needed [39], [40], [41].

III. DEVICE FABRICATION AND CHARACTERIZATION

Our PBS devices is fabricated using a commercial z-cut LNTF (NANOLN) with a LN layer of 800 nm thick, a 2- μm silica layer, and a 500- μm silicon substrate. The preparation process of the structure mainly follows three steps. Firstly, a 665-nm thick amorphous silicon is deposited as the hard etching mask for LN by plasma-enhanced chemical vapor deposition (PECVD). Next, a layer of resist is spin-coated on the surface of amorphous silicon. The mask is defined via electron beam lithography (EBL). The pattern is then directly transferred to the silicon mask and the LNTF sample by argon-based inductive coupling plasmon (ICP) etching. Finally, the residual silicon mask is removed by KOH solution. The chip facets are polished for lensed fiber coupling.

Fig. 5 shows the experimental setup for the device characterization. To investigate the operation of the PBS, a tunable laser source (New Focus, 1520–1570 nm), whose polarization is controlled by a polarization controller (PC), is coupled to the input waveguide of the PBS through a lensed fiber (LF). For output mode characterization, light from the output facet

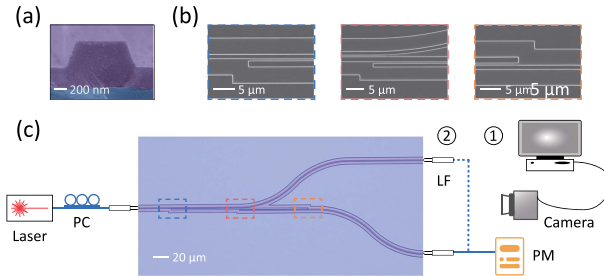


Fig. 5. (a) Cross section of the waveguide. (b) Enlarged view of the corresponding areas marked in (c). (c) Optical microscopy image of the PBS device and the characterization experimental setup.

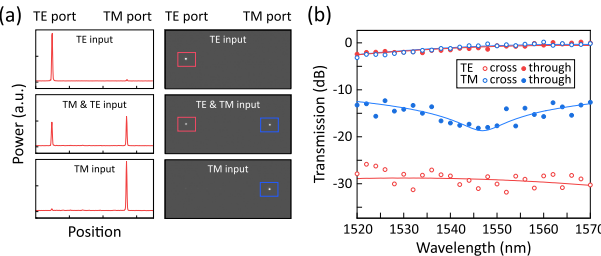


Fig. 6. (a) The intensity distribution and the mode profiles observed in the infrared CCD at different input polarization states, i.e., TE, TE&TM, TM input. (b) Measured transmission spectra of the TE and TM ports for TE or TM mode input.

of the chip is directly imaged using an objective lens and an infrared CCD. Figures 5(a) and 5(b) shows the scanning electron microscope (SEM) images of the cross section of the input waveguide and marked zones in the microscope image of the fabricated PBS device in Fig. 5(c). The actual etching depth is measured to be approximately 440 nm, consistent with the design parameter. The effective length of the PBS, $2L_c$ is only 180 μm . The output channels are 125 μm apart after introducing the two S-bend waveguides to separate the two ports for the convenience during experimental measurement.

As shown in Fig. 6, our PBS could efficiently split the input light into the two orthogonally polarized output ports. Fig. 6(a) displays the intensity distribution (left column) and the mode profiles (right column) of the output channels with different input polarization states as observed in the infrared CCD. Obviously, the TE and TM modes are well separated by the PBS. During the experiment, the polarization states of the input and the designated output ports have also been checked by a polarization analyzer.

For qualitative characterization, we replace the imaging system with a second lensed fiber to collect the light of each output ports. The out coupled light power is monitored using an InGaAs powermeter for one output port at a time. By varying the input polarization states, the maximum and minimum power of the through and cross ports are respectively obtained by the PM. The obtained result is shown in Fig. 6(b). The on-chip insertion loss of the PBS for TE and TM mode input is approximately 1.10 dB and 1.24 dB at 1550 nm, respectively. The measured PER for TE and TM exceeds 26 dB and 13 dB, respectively, in the 1520–1570 nm range (limited by the laser source). The TM extinction ratio is smaller than theoretical prediction mainly

due to a small deviation of the etching depth from the optimized result. In addition, the splitting process for the TM mode involves mode cross-coupling and the condition is not far from strong mode hybridization. As shown in Fig. 4(b), the TM mode will obtain a very high extinction ratio only under the exact phase matching condition. Still, our fabricated PBS has a good performance in terms of polarization splitting as compared with the current similar work [30], [31], [32], [33], [34], [35], [36].

IV. CONCLUSION

In conclusion, we design and demonstrate a compact PBS on LNTF two ADCs with an effective length of only 180 μm . A good PER exceeding 26 dB and 13 dB for respective TE_0 and TM_0 modes over the whole telecom-C band is experimentally obtained. The device has a simple structure and only requires a single-step EBL and ICP etching process. The device holds promise for efficient on-chip polarization division multiplexing or polarization manipulation. It expands the toolbox on the LNTF platform and would become an indispensable component in future PICs.

ACKNOWLEDGMENT

We would like to thank the Center for Advanced Electronic Materials and Devices (AEMD) of Shanghai Jiao Tong University for the assistances of device fabrication.

REFERENCES

- [1] A. Boes, B. Corcoran, L. Chang, J. Bowers, and A. Mitchell, "Status and potential of lithium niobate on insulator (Inoi) for photonic integrated circuits," *Laser Photon. Rev.*, vol. 12, no. 4, 2018, Art. no. 1700256. [Online]. Available: <https://onlinelibrary.wiley.com/doi/abs/10.1002/lpor.201700256>
- [2] D. Zhu et al., "Integrated photonics on thin-film lithium niobate," *Adv. Opt. Photon.*, vol. 13, no. 2, pp. 242–352, Jun. 2021. [Online]. Available: <http://opg.optica.org/aop/abstract.cfm?URI=aop-13-2-242>
- [3] Y. Zheng and X. Chen, "Nonlinear wave mixing in lithium niobate thin film," *Adv. Phys.: X*, vol. 6, no. 1, 2021, Art. no. 1889402. [Online]. Available: <https://doi.org/10.1080/23746149.2021.1889402>
- [4] J. Lin, F. Bo, Y. Cheng, and J. Xu, "Advances in on-chip photonic devices based on lithium niobate on insulator," *Photon. Res.*, vol. 8, no. 12, pp. 1910–1936, Dec. 2020. [Online]. Available: <http://opg.optica.org/prj/abstract.cfm?URI=prj-8-12-1910>
- [5] S. Saravi, T. Pertsch, and F. Setzpfandt, "Lithium niobate on insulator: An emerging platform for integrated quantum photonics," *Adv. Opt. Mater.*, vol. 9, no. 22, 2021, Art. no. 2100789. [Online]. Available: <https://onlinelibrary.wiley.com/doi/abs/10.1002/adom.202100789>
- [6] X. Chen, Z. Fu, Q. Gong, and J. Wang, "Quantum entanglement on photonic chips: A review," *Adv. Photon.*, vol. 3, no. 6, pp. 1–8, 2021. [Online]. Available: <https://doi.org/10.1111/1.AP.3.6.064002>
- [7] C. Wang et al., "Integrated lithium niobate electro-optic modulators operating at CMOS-compatible voltages," *Nature*, vol. 562, pp. 101–104, 2018. [Online]. Available: <https://doi.org/10.1038/s41586-018-0551-y>
- [8] C. Wang et al., "Ultrahigh-efficiency wavelength conversion in nanophotonic periodically poled lithium niobate waveguides," *Optica*, vol. 5, no. 11, pp. 1438–1441, Nov. 2018. [Online]. Available: <http://opg.optica.org/optica/abstract.cfm?URI=optica-5-11-1438>
- [9] J. Zhao et al., "Shallow-etched thin-film lithium niobate waveguides for highly-efficient second-harmonic generation," *Opt. Exp.*, vol. 28, no. 13, pp. 19669–19682, Jun. 2020. [Online]. Available: <http://opg.optica.org/oe/abstract.cfm?URI=oe-28-13-19669>
- [10] J. Lu et al., "Periodically poled thin-film lithium niobate microring resonators with a second-harmonic generation efficiency of 250,000%/w," *Optica*, vol. 6, no. 12, pp. 1455–1460, Dec. 2019. [Online]. Available: <http://opg.optica.org/optica/abstract.cfm?URI=optica-6-12-1455>

- [11] S. Liu, Y. Zheng, Z. Fang, X. Ye, Y. Cheng, and X. Chen, "Effective four-wave mixing in the lithium niobate on insulator microdisk by cascading quadratic processes," *Opt. Lett.*, vol. 44, no. 6, pp. 1456–1459, Mar. 2019. [Online]. Available: <http://opg.optica.org/ol/abstract.cfm?URI=ol-44-6-1456>
- [12] X. Ye, S. Liu, Y. Chen, Y. Zheng, and X. Chen, "Sum-frequency generation in lithium-niobate-on-insulator microdisk via modal phase matching," *Opt. Lett.*, vol. 45, no. 2, pp. 523–526, Jan. 2020. [Online]. Available: <http://opg.optica.org/ol/abstract.cfm?URI=ol-45-2-523>
- [13] Y. He et al., "Self-starting bi-chromatic linbo₃ soliton microcomb," *Optica*, vol. 6, no. 9, pp. 1138–1144, Sep. 2019. [Online]. Available: <http://opg.optica.org/optica/abstract.cfm?URI=optica-6-9-1138>
- [14] M. Yu, B. Desiatov, Y. Okawachi, A. L. Gaeta, and M. Lončar, "Coherent two-octave-spanning supercontinuum generation in lithium-niobate waveguides," *Opt. Lett.*, vol. 44, no. 5, pp. 1222–1225, Mar. 2019. [Online]. Available: <http://opg.optica.org/ol/abstract.cfm?URI=ol-44-5-1222>
- [15] J. Zhao, C. Ma, M. Rüsing, and S. Mookherjea, "High quality entangled photon pair generation in periodically poled thin-film lithium niobate waveguides," *Phys. Rev. Lett.*, vol. 124, Apr. 2020, Art. no. 163603. [Online]. Available: <https://link.aps.org/doi/10.1103/PhysRevLett.124.163603>
- [16] M. He et al., "High-performance hybrid silicon and lithium niobate Mach-Zehnder modulators for 100 Gbit · s⁻¹ and beyond," *Nat. Photon.*, vol. 13, pp. 359–364, 2019. [Online]. Available: <https://doi.org/10.1038/s41566-019-0378-6>
- [17] M. Li, J. Ling, Y. He, U. A. Javid, S. Xue, and Q. Lin, "Lithium niobate photonic-crystal electro-optic modulator," *Nat. Commun.*, vol. 11, 2020, Art. no. 4123. [Online]. Available: <https://doi.org/10.1038/s41467-020-17950-7>
- [18] X. Sun et al., "Experimental investigation on the unbalanced mach-Zehnder interferometer on lithium niobate thin film," *Chin. Opt. Lett.*, vol. 20, no. 10, 2022, Art. no. 101301.
- [19] X. Liu et al., "Broadband meandered thin-film lithium niobate modulator with ultra-low half-wave voltage," *IEEE Photon. Technol. Lett.*, vol. 34, no. 8, pp. 424–427, Apr. 2022.
- [20] J. Cai, C. Guo, C. Lu, A. P. T. Lau, P. Chen, and L. Liu, "Design optimization of silicon and lithium niobate hybrid integrated traveling-wave Mach-Zehnder modulator," *IEEE Photon. J.*, vol. 13, no. 4, Aug. 2021, Art. no. 2200206.
- [21] L. Yu et al., "Design of high-speed mid-infrared electro-optic modulator based on thin film lithium niobate," *IEEE Photon. J.*, vol. 14, no. 2, Apr. 2022, Art. no. 6621506.
- [22] J. Lu, A. A. Sayem, Z. Gong, J. B. Surya, C.-L. Zou, and H. X. Tang, "Ultralow-threshold thin-film lithium niobate optical parametric oscillator," *Optica*, vol. 8, no. 4, pp. 539–544, Apr. 2021. [Online]. Available: <http://opg.optica.org/optica/abstract.cfm?URI=optica-8-4-539>
- [23] M. Zhang et al., "Broadband electro-optic frequency comb generation in a lithium niobate microring resonator," *Nature*, vol. 568, pp. 373–377, 2019. [Online]. Available: <https://doi.org/10.1038/s41586-019-1008-7>
- [24] M. Xu, M. He, Y. Zhu, S. Yu, and X. Cai, "Flat optical frequency comb generator based on integrated lithium niobate modulators," *J. Lightw. Technol.*, vol. 40, no. 2, pp. 339–345, 2022.
- [25] J. Lu, J. B. Surya, X. Liu, Y. Xu, and H. X. Tang, "Octave-spanning supercontinuum generation in nanoscale lithium niobate waveguides," *Opt. Lett.*, vol. 44, no. 6, pp. 1492–1495, Mar. 2019. [Online]. Available: <http://opg.optica.org/ol/abstract.cfm?URI=ol-44-6-1492>
- [26] G. Chen et al., "Four-channel CWDM device on a thin-film lithium niobate platform using an angled multimode interferometer structure," *Photon. Res.*, vol. 10, no. 1, pp. 8–13, Jan. 2022. [Online]. Available: <http://opg.optica.org/prj/abstract.cfm?URI=prj-10-1-8>
- [27] X. Han et al., "Mode and polarization-division multiplexing based on silicon nitride loaded lithium niobate on insulator platform," *Laser Photon. Rev.*, vol. 16, no. 1, 2022, Art. no. 2100529. [Online]. Available: <https://onlinelibrary.wiley.com/doi/abs/10.1002/lpor.202100529>
- [28] M. Xu et al., "Dual-polarization thin-film lithium niobate in-phase quadrature modulators for terabit-per-second transmission," *Optica*, vol. 9, no. 1, pp. 61–62, Jan. 2022. [Online]. Available: <http://opg.optica.org/optica/abstract.cfm?URI=optica-9-1-61>
- [29] D. Dai, L. Liu, S. Gao, D.-X. Xu, and S. He, "Polarization management for silicon photonic integrated circuits," *Laser Photon. Rev.*, vol. 7, no. 3, pp. 303–328, 2013. [Online]. Available: <https://onlinelibrary.wiley.com/doi/abs/10.1002/lpor.201200023>
- [30] Z. Chen, J. Yang, W.-H. Wong, E. Y.-B. Pun, and C. Wang, "Broadband adiabatic polarization rotator-splitter based on a lithium niobate on insulator platform," *Photon. Res.*, vol. 9, no. 12, pp. 2319–2324, Dec. 2021. [Online]. Available: <http://opg.optica.org/prj/abstract.cfm?URI=prj-9-12-2319>
- [31] X. Wang, A. Pan, T. Li, C. Zeng, and J. Xia, "Efficient polarization splitter-rotator on thin-film lithium niobate," *Opt. Exp.*, vol. 29, no. 23, pp. 38044–38052, Nov. 2021. [Online]. Available: <http://opg.optica.org/oe/abstract.cfm?URI=oe-29-23-38044>
- [32] H. Luo et al., "High-performance polarization splitter-rotator based on lithium niobate-on-insulator platform," *IEEE Photon. Technol. Lett.*, vol. 33, no. 24, pp. 1423–1426, Dec. 2021.
- [33] G. Yang, A. V. Sergienko, and A. Ndao, "Plasmonic loss-mitigating broadband adiabatic polarizing beam splitter," *Opt. Lett.*, vol. 47, no. 3, pp. 629–632, Feb. 2022. [Online]. Available: <http://opg.optica.org/ol/abstract.cfm?URI=ol-47-3-629>
- [34] S. Mao, L. Cheng, C. Zhao, and H. Y. Fu, "Ultra-broadband and ultra-compact polarization beam splitter based on a tapered subwavelength-grating waveguide and slot waveguide," *Opt. Exp.*, vol. 29, no. 18, pp. 28066–28077, Aug. 2021. [Online]. Available: <http://opg.optica.org/oe/abstract.cfm?URI=oe-29-18-28066>
- [35] L. Zhang, L. Zhang, X. Fu, and L. Yang, "Compact, broadband and low-loss polarization beam splitter on lithium-niobate-on-insulator using a silicon nanowire assisted waveguide," *IEEE Photon. J.*, vol. 12, no. 5, Oct. 2020, Art. no. 6601906.
- [36] H.-P. Chung et al., "Broadband on-chip polarization mode splitters in lithium niobate integrated adiabatic couplers," *Opt. Exp.*, vol. 27, no. 2, pp. 21632–21645, Jan. 2019. [Online]. Available: <http://opg.optica.org/oe/abstract.cfm?URI=oe-27-2-1632>
- [37] T. Wang et al., "Cross-polarization generation and its impact on coupler performance," *IEEE J. Sel. Topics Quantum Electron.*, vol. 12, no. 4, pp. 2751–2759, Jul./Aug. 2006.
- [38] A. Pan, C. Hu, C. Zeng, and J. Xia, "Fundamental mode hybridization in a thin film lithium niobate ridge waveguide," *Opt. Exp.*, vol. 27, no. 24, pp. 35659–35669, Nov. 2019. [Online]. Available: <http://opg.optica.org/oe/abstract.cfm?URI=oe-27-24-35659>
- [39] H. Xu, D. Dai, L. Liu, and Y. Shi, "Proposal for an ultra-broadband polarization beam splitter using an anisotropy-engineered mach-zehnder interferometer on the X-cut lithium-niobate-on-insulator," *Opt. Exp.*, vol. 28, no. 8, pp. 10899–10908, Apr. 2020. [Online]. Available: <http://opg.optica.org/oe/abstract.cfm?URI=oe-28-8-10899>
- [40] C. Deng et al., "Broadband and compact polarization beam splitter in LNOI hetero-anisotropic metamaterials," *Opt. Exp.*, vol. 29, no. 8, pp. 11627–11634, Apr. 2021. [Online]. Available: <http://opg.optica.org/oe/abstract.cfm?URI=oe-29-8-11627>
- [41] X. Shi et al., "Compact low-birefringence polarization beam splitter using vertical-dual-slot waveguides in silicon carbide integrated platforms," *Photon. Res.*, vol. 10, no. 1, pp. A8–A13, Jan. 2022. [Online]. Available: <http://opg.optica.org/prj/abstract.cfm?URI=prj-10-1-A8>